JOURNAL OF SPACECRAFT AND ROCKETS
Vol. 48, No. 1, January–February 2011

Electromagnetic Formation Flight Testbed Using Superconducting Coils

Daniel W. Kwon[*] and Raymond J. Sedwick[†]
University of Maryland, College Park, Maryland 20742
and
Sang-il Lee[‡] and Jaime L. Ramirez-Riberos[§]
Massachusetts Institute of Technology, Cambridge, Massachusetts 02139

DOI: 10.2514/1.45017

An alternative actuation system for formation flight spacecraft uses electromagnetic force generated by an electromagnetic dipole in concert with reaction wheels to control the position and attitude of each satellite relative to each other. This novel concept is called electromagnetic formation flight. All the actuators in the system are powered by solar energy and the formation flight propulsion system does not depend on consumables. To demonstrate electromagnetic formation flight a proof-of-concept ground testbed is developed. This paper describes the design of the testbed vehicles and the first known closed-loop control of electromagnetic formation flight vehicles. Demonstrations involving position hold and trajectory following maneuvers show that standard control approaches can be used to control the motion of a formation flying testbed using unique electromagnet actuation system.

Nomenclature

A = amplitude of desired trajectory
A_c = area enclosed by coil
$\mathbf{B}$ = magnetic field
F_f = motor friction
F_x = electromagnetic force applied to a moving vehicle along x
F_y = electromagnetic force applied to a moving vehicle along y
f = frequency of desired trajectory
I_w = inertia of reaction wheel
I_z = inertia of moving vehicle
i = current
$\mathbf{K}_k$ = extended Kalman filter gain
$\mathbf{K}_{\mathrm{LQR}}$ = control gain
$\mathbf{K}_\theta$ = control gain for attitude controller
K_d = derivative gain for attitude controller
K_i = integral gain for attitude controller
K_p = proportional gain for attitude controller
K_t = torque constant of a motor
M = vehicle mass
N = number of turns
R_A = motor armature resistance
r = distance between vehicles
T_{RW} = torque generated by reaction wheel
T = electromagnetic torque
$\mathbf{u}$ = control input vector
V = voltage applied to a motor
V_{emf} = counterelectromotive force voltage of a motor
x = position coordinate of vehicle in axial direction
x_b = body-fixed coordinate for moving vehicle
$\boldsymbol{x}$ = state vector
$\hat{\mathbf{x}}$ = state estimate vector
y = position coordinate of vehicle in shear direction
y_b = body-fixed coordinate for moving vehicle
$\mathbf{z}$ = measurement vector
$\tilde{\mathbf{z}}$ = modified measurement vector
θ = attitude angle
μ = magnetic dipole strength
μ_o = permeability of free space, $4\pi \cdot 10^{-7}\ \mathrm{T \cdot m/A}$
μ_1 = dipole strength of a moving vehicle along x_b
μ_2 = dipole strength of a moving vehicle along y_b
ω = angular velocity of a reaction wheel

Subscripts

d = desired trajectory
k = time step
M = moving vehicle
S = stationary vehicle

I. Introduction

MULTIPLE spacecraft flown in formation can potentially provide several advantages over larger traditional satellites systems. The overall concept is that a formation of smaller satellites can gather not only more data, but higher quality data than a single monolithic satellite. One example is using multiple spacecraft for space-based interferometery such as ESA's Darwin mission [1]. Without the size constraints imposed by launch vehicles, large sensor apertures can be created enabling a system with increased angular resolution. Also, small spacecraft provide potential cost savings in manufacturing, packaging and launch. A mission consisting of multiple spacecraft allows for staged deployment and can be upgraded by replacing the necessary spacecraft instead of replacing the entire system. There is also opportunity for modular design in formation flight or the use of fractionated spacecraft architectures that could lead to lower cost and more effective and responsive missions [2].

One of the challenges for formation flying systems is maintaining precise control over each spacecraft in the array while minimizing fuel use. Using traditional thrusters the amount of fuel needed can become prohibitively large as the mission lifetime increases, especially for formation flight applications that require controlling

---

Received 16 September 2009; revision received 24 October 2010; accepted for publication 27 October 2010.

[*] Faculty Research Assistant, Department of Aerospace Engineering, 3181 Martin Hall. Member AIAA.

[†] Assistant Professor, Department of Aerospace Engineering, 3181 Martin Hall. Associate Fellow AIAA.

[‡] Graduate Student, Department of Aeronautics and Astronautics, 77 Massachusetts Ave. Room 35-217. Student Member AIAA.

[§] Graduate Student, Department of Aeronautics and Astronautics, 77 Massachusetts Ave. Room 35-340. Student Member AIAA.

individual satellites positions with very small error, such as sparse aperture arrays. Since formations of spacecraft rely on relative positions of their elements, savings could be made by using interaction forces between the vehicles. One method is to create an external field on each satellite in the array by which other satellites can react against. As a result, the need for fuel for formation flying maneuvers is obviated. One technique developed by Schaub is to use electrostatic forces [3]. By building up charge on the various vehicles, attraction and repulsion forces are created. This concept of using Coulomb forces enables novel formation flying structures in high Earth orbit. A one-dimensional testbed has demonstrated a proof-of-concept Coulomb spacecraft [4].

A second method is to use electromagnetic forces and in this paper is called electromagnetic formation flight (EMFF). This paper first gives an overview of EMFF and an experimental EMFF ground testbed. Prior work on hardware-in-the-loop spacecraft formation flying testbeds and application of LQR control and Kalman filter estimation has been conducted by Mitchell et al. [5], Monda and Schaub [6], and Veres et al. [7]. A testbed developed by Romano and Hall for autonomous spacecraft assembly and reconfiguration used an air bearing system on a flat floor [8]. This setup is similar to the EMFF testbed which is described in Sec. III. Section IV introduces the dynamics and control for a formation flying testbed using electromagnetic actuators. To demonstrate the operation of the EMFF testbed position hold and trajectory following tests were conducted. The results show successful application of standard control techniques applied to novel hardware. The paper describes a unique demonstration of closed-loop two-dimensional control of objects using electromagnetic fields. This system is a promising new type of actuator for future formation flying missions.

II. Overview

An example of forces created by two EMFF spacecraft is attraction or repulsion. This is created by axially aligning to magnetic dipoles, where each spacecraft creates its own magnetic dipole. In addition, shear forces are created by aligning the fields orthogonal to each other. In this technique the forces and torques are coupled. Simple examples of attraction and shear motions are shown in Fig. 1. A coil of wire with current is implemented to create a magnetic dipole. The strength of the electromagnet is controlled by varying the amount of current in the coil. For a spacecraft containing three orthogonal coils, an effective dipole can be steered in three dimensions. To decouple the forces and torques reaction wheels are used. Using three orthogonal reaction wheels, all relative degrees of freedom can be controlled. One important control consideration for EMFF is that to move the center of mass of the satellite array, a propellant-based system must be used. It has also been proposed by Schweighart [9] to move an EMFF array by reacting against the Earth's magnetic field.

One of the advantages of EMFF over propellant-based thrusters is that the satellite array does not rely on a consumable resource. Electromagnetic forces are produced using electric current which is generated from solar energy using solar panels. This allows the spacecraft's lifetime to be limited by its hardware life instead of by the amount of fuel on board. Another advantage is the elimination of thruster plumes which can potentially impinge nearby objects. This is advantageous for formation flying space telescopes especially infrared imaging missions since a hot propellant plume caused by electric propulsion options such as field emission electric propulsion can obscure observations [10].

There are several relevant areas of background and previous work for EMFF. The first area is previous dynamics and control research using EMFF. Elias developed a nonlinear dynamics model for two spacecraft with electromagnets and reaction wheels including reaction wheel gyroscopic stiffening effects [11]. A linearized dynamics model was used to simulate the steady-state rotation of two EMFF satellites that were part of a deep-space interferometer. A linear quadratic regulator (LQR) controller showed stability of the closed-loop system. Wawrzaszek and Banaszkiewicz extended the two vehicle nonlinear controller developed by Elias to a three vehicle linear array and a three vehicle triangular array [12]. Ahsun devised nonlinear adaptive control laws and angular momentum management by switching dipole polarity for operating EMFF on n-spacecraft in low Earth orbit [13]. Schweighart considered n-spacecraft, for which the equations of motion, described as polynomial functions of the magnetic dipole of each satellite, were solved [9]. Additionally, angular momentum management and operation under the Earth's gravitational field, including the J_2 disturbance and magnetic field were investigated.

The EMFF testbed described in this paper is developed from trade studies by Kong et al. [14]. Superconducting wire is an enabling technology since it allows for the creation of a large magnetic moment. This provides micropropulsion level thrust in the tens of milli-Newtons at several hundred meters separation. Conventional wire is not able to carry a large current continuously necessary for missions requiring separation beyond several meters. High-temperature superconducting (HTS) wire has been developed that is capable of carrying over 140 times the current of copper wires of the same size. One of the challenges of implementing HTS coils is that the wire must be cooled to temperatures below the critical temperature to be superconductive. Immersion in liquid nitrogen is one solution for a ground testbed, however, current research has considered using cryocoolers and cryogenic heat pipes for a flight thermal system.

III. Testbed Description

As a proof-of-concept for EMFF, a testbed consisting of two vehicles is designed and built. The vehicles are designed so that one vehicle can perform a circular trajectory on a flat table with size approximately 2 by 1 m in two to 3 min. In addition, the force

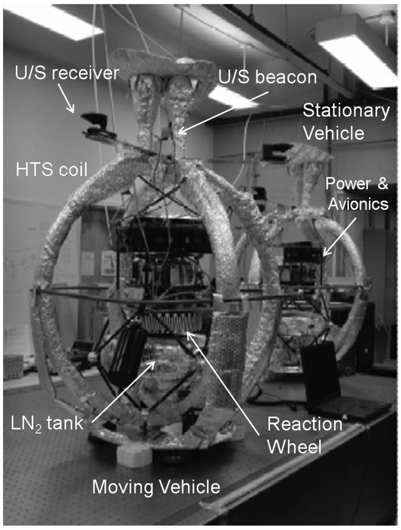

Fig. 2 Electromagnetic formation flight testbed.

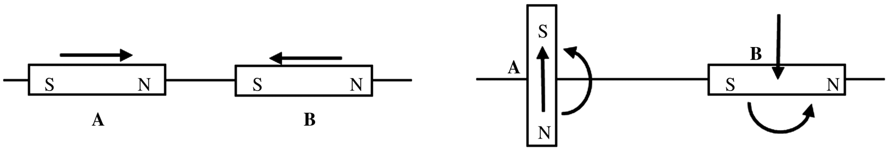

Fig. 1 Forces and torques between two dipoles.

Table 1 Mass and moment of inertia for EMFF vehicle

Component	Mass, kg	Radius, m	Moment of inertia, $kg \cdot m^2$
Large coil	9.00	0.425	0.82
Small coil	8.00	0.395	0.63
Tank, LN_2	9.25	0.198	0.18
Structural ring	0.75	0.450	0.08
Other	9.00	0.200	0.18
Total	36.00		1.89

generated must be able to overcome friction forces. The overall design of the vehicles is based on a previous generation EMFF testbed that demonstrated open-loop attraction, repulsion, and shear forces. The goal of this version of the testbed is to demonstrated closed-loop control of the vehicles. To simplify the testing scenarios the EMFF testbed consists of one moving vehicle and one stationary vehicle placed on a flat table as shown in Fig. 2. The two vehicles are identical except for the air bearing system on the moving vehicle. The air bearing system consists of two 16 oz tanks of CO_2 and three New Way air bearing pucks allowing for a total float time of approximately 20 min. The mass of an EMFF vehicle is approximately 36 kilograms when full of liquid nitrogen (LN_2). The physical properties such as the mass and moment of inertia are listed in Table 1 [15]. The three main subsystems for the EMFF vehicles are the actuators, avionics, and metrology system. Since the EMFF testbed uses a unique actuation system, detailed system engineering issues of each of the subsystems are given in the following subsections. Even though there are several custom built components, a significant portion of the vehicles use commercial-off-the-shelf (COTS) hardware.

A. Actuators

To demonstrate maneuvers in a two-dimensional plane, each vehicle has two superconducting coils arranged orthogonally to each other for position control. Located in the center of the vehicle is a single reaction wheel for attitude control.

1. Superconducting Coils

The superconducting coil assembly is made of Bi-2223 High Strength Wire,[¶] which is COTS wire from American Superconductor. To maintain a temperature below the HTS wire critical temperature of 110 K, the superconducting wire resides inside a copper container, which is filled with liquid nitrogen, which has a temperature of 77 K. The two orthogonal coils are slightly different in size. The outer coil has 99 turns and a diameter of 32.9 in., and the inner coil has 103 turns and a diameter of 30.6 in.. The copper container and a liquid nitrogen reservoir system are pressurized and are designed to hold enough LN_2 for approximately 20 min [15]. Insulation, which can be seen in Fig. 2, is wrapped around the copper container to minimize LN_2 boiloff.

Superconducting wire allows for high strength magnetic fields to be created by enabling the coils to carry a high current. The magnetic moment is a function of current and the force created increases with current squared. One of the engineering challenges is providing an umbilical-less power system for the HTS coils. The HTS coil acts as a large inductor with zero resistance in a circuit while it is superconducting. Current through the coil, not the voltage, is the critical factor and for low power consumption the voltage is kept relatively low. The only resistance in the circuit occurs in the internal resistance of the power system components such as the batteries, wiring, and MOSFETs or switches. Therefore, the design of the power system must minimize this internal resistance, but also be capable of supplying high current at low voltages with enough accuracy to satisfy control requirements. In addition, since the magnetic field must have the ability to switch polarity, the current through the coil must be driven both in forward and reverse directions.

The power system that meets these requirements is an H-bridge design where the electromagnet is the typical load for the H-bridge, which allows for the current to be driven in either direction through the coil. A current sensor in series with the electromagnet is used to measure the coil current and logic hardwired into a power circuit is used to regulate the current flow. The H-bridge MOSFET driver is the HIP4081A made by Texas Instruments, the current sensor is the ACS750 made by Allegro, and the MOSFETs used are the HUF7614 made by Fairchild Semiconductor. The current source for the system is a set of high energy density Nickel Metal Hydride D-cell batteries, which can provide 45 amps of continuous current discharge and up to 120 amps momentarily. The power consumption during operation is approximately 55 watts while operating at a current of 85 amps. One of the challenges operating an EMFF testbed is that it is important to ensure that the entire wires making up the coil are sufficiently submerged in liquid nitrogen while driving current to prevent the HTS wire from burning out, which occurred during one initial test [15].

2. Reaction Wheel

The reaction wheel assembly (RWA) consists of a permanent magnet motor with a gear box, a custom urethane reaction wheel, a motor control unit, and a tachometer for measuring the angular speed of the reaction wheel. The permanent magnet motor is an Astro 40 Cobalt Geared Motor by Astro Flight, Inc. The motor control unit is an Astro 30 Amp Reversing Marine Speed Control by Astro Flight, Inc., which takes a pulse width modulation signal from the flight computer as an input, and provides the motor with a voltage. The reaction wheel is made of urethane, a nonmetallic material, to avoid any potential problems with eddy currents that may arise when rotating a large metal disk in a magnetic field. As a tradeoff, a urethane reaction wheel has less angular momentum storage than a metal reaction wheel of the same shape and size. One of the challenges of implementing the reaction wheel has been generating sufficient angular momentum. During some of the initial open-loop and closed-loop tests with the two EMFF vehicles there was insufficient angular momentum generated by the reaction wheel. During the tests the RWA would lose authority for attitude control. One initial solution was to double the moment of inertia of the reaction wheel, from $0.01\ kg \cdot m^2$ to $0.02\ kg \cdot m^2$ by simply attaching an identical wheel to the same motor shaft. Experimental tests shown later in this paper show that this is a successful solution for most maneuvers, but one that still requires improvement.

B. Avionics

The computer subsystem is responsible for taking metrology measurements, commanding the actuators, communicating between the vehicles and a laptop ground station, and implementing the control and estimation algorithms. The computer subsystem was originally built for the SPHERES (synchronized position-hold, engage, reorient experimental satellites) project [16] and the flow of

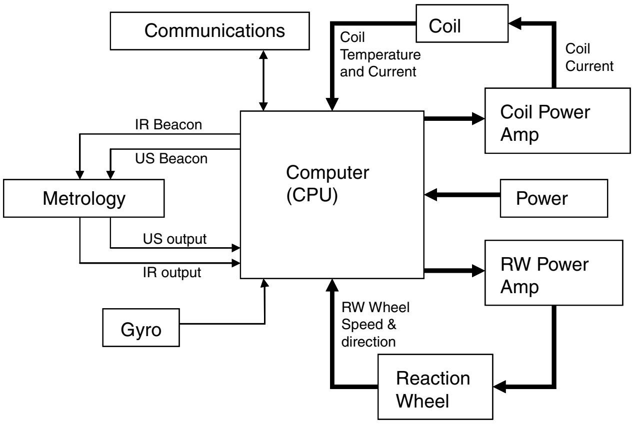

Fig. 3 Avionics diagram.

[¶] Data available online at http://www.amsuper.com/ [retrieved 10 September 2009].

data into and out of the system is summarized in Fig. 3. A Texas Instruments C6701 DSP runs the testbed software at a rate of 167 MHz. Analog sensors are sampled and digitized by an FPGA at 12-bit resolution at a speed of 25 MHz. The computer obtains information from the reaction wheel tachometer, a gyroscope, a temperature sensor, and a current sensor. The computer outputs commands to the actuators, which are the reaction wheel and electromagnetic coils. The communications subsystem uses a radio frequency channel to transmit data. An RF Monolithics DR2000 board is used for communication between the vehicles and a ground station and it employs a radio frequency signal of 916.5 MHz with data rate of 57.6 kbps. The communication protocol of the testbed is a token ring network with three stations consisting of the two testbed vehicles and one laptop.

One of the concerns of EMFF is possible adverse effects of the magnetic fields on electronics. A separate experiment to assess the performance of avionics in the presence of EMFF fields was conducted using Global Positioning System (GPS) equipment. The preliminary results indicate that a 50 Gauss magnetic field, which is produced by a single coil and is representative of the field strength during experiments, does not impact the signal to noise ratio obtained by the GPS receiver [17]. In addition, there have been no known problems operating the computer system during tests. One area of ongoing research is to obtain more quantitative results, to determine the effect, if any, of the magnetic field on the number of instructions per second by the microprocessor and the effect, if any, of the magnetic field on the bits per second transmitted by the communications boards. If operating avionics is a problem, placing sensitive electronics inside a mu metal box is a proposed solution.

C. Metrology System

To determine the relative positioning of the EMFF vehicles a time of flight measurement system using infrared and ultrasound (U/S) beacons and receivers is used. Each vehicle has both infrared and U/S metrology and a rate gyro to obtain knowledge of its position, velocity, and attitude. The rate gyro is a BEI GyroChip II made by BEI Technology, Inc. The U/S metrology consists of one beacon and three receivers and their geometry is shown in Fig. 4. The beacon generates ultrasound pulses with a known period, and the receivers detect ultrasound during a defined time window. To measure the separation distance between two vehicles, first both vehicles are synchronized by an infrared signal at the beginning of a control period. Next, the beacon of the stationary vehicle generates a U/S pulse while its receivers are inactive. The receivers of the moving vehicle detect the U/S pulse, and calculate the time of flight for each receiver, which is used to determine the separation distance. This value is stored by the moving vehicle. Then, the beacon of the moving vehicle generates a U/S pulse with its receivers dormant. The receivers of the stationary vehicle detect the U/S pulse, and this distance measurement is calculated and stored by the stationary vehicle. The state vector is composed of x position and velocity, y position and velocity, and the vehicle angle and angular rate. The metrology system is capable of determining position within 1 cm and operates at 1 Hz.

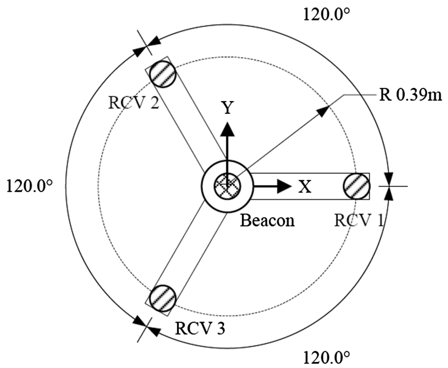

Fig. 4 Geometry of ultrasound metrology system (top view).

There were several lessons learned while implementing the relative positioning metrology system. As the system was initially designed, it was difficult to obtain consistent, accurate measurements. The estimator uses the measurement vector $\mathbf{z}_k = [x_k \quad y_k \quad \theta_k \quad \dot{\theta}_k]^T$ where the first three elements are nonlinear functions of the six ultrasound measurements. Occasionally some of the six ultrasound measurements at t_k were incorrect or missed corrupting $\mathbf{z}_k$ and causing the estimator to provide unreasonable estimated state variables for the LQR controller.

There were two sources for the problem. First, liquid nitrogen boiloff from the chimneys standing next to the U/S beacon enveloped the beacon with a cold cloud of vapor causing the oscillator to stiffen. This shifted the frequency of the transmitted ultrasound signal out of a range that is detectable by the U/S receivers leading to dropped measurement data. To resolve this problem the LN_2 chimneys, which are shown in Fig. 2, are equipped with umbrellas that uniformly spread the boiloff away from the beacons. Directing the boiloff away using an exhaust-type system was avoided since it could add disturbances and act as a propulsion system. A second problem with the metrology system was the location of the U/S receivers. For certain vehicle attitudes, one of the three U/S receivers in one vehicle did not have direct line of sight of the U/S beacon on the other vehicle, partly due to blockage from the LN_2 chimney and umbrella setup. As a solution the attitude of the moving vehicle was constrained so that maneuvers allowed for direct line of sight between the metrology systems of each vehicle, if possible.

Two steps were taken to improve the accuracy of $\mathbf{z}_k$. The first solution was to replace the current state estimate, if corrupted by bad measurements, with the previous state estimate. The estimator replaces the state estimate at t_k, $\hat{x}_k$, with the state estimate at t_{k-1}, $\hat{x}_{k-1}$, if any element of $\hat{x}_k$ is considerably different than the corresponding element of $\hat{x}_{k-1}$. The second step was to move the U/S beacon from the stationary vehicle off the vehicle. During tests, it was observed that the variation of the U/S range measurements were less sensitive to a change in the shear or y-direction compared with changes in the axial or x-direction for all six U/S receivers since most maneuvers were dominated by axial maneuvers. This resulted in more noisy estimates of y and $\dot{y}$ than those of x and $\dot{x}$. To better capture motion along the y-direction, the beacon was moved to a location 1.5 m away from the moving vehicle in both the x and y directions as shown in Fig. 5. As a result the estimates of y and $\dot{y}$ improved and allowed for more consistent testing. A future design consideration that could have avoided some of the challenges associated with the relative metrology system is to implement an absolute positioning metrology system with all beacons off the vehicles completely and to simulate the relative position and attitude information from the absolute estimates.

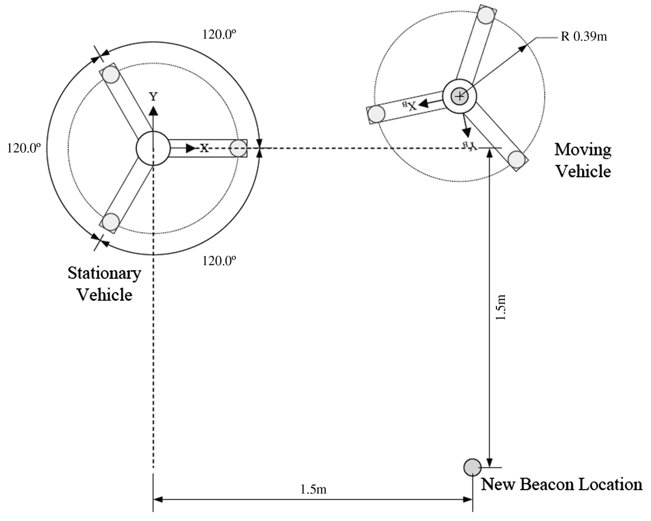

Fig. 5 Vehicle and metrology configuration during testing.

IV. Dynamics and Control

A. Equations of Motion

At distances far from a coil of current, the magnetic field looks similar to one created by a magnetic dipole or a permanent magnet with a north and south pole. The dipole points through the center of the coil, with its direction determined by the right-hand rule. The magnetic moment or strength dipole is determined by the current in the wire, the number of turns of wire, and the area enclosed by the coil

$$\mu = NiA_c \tag{1}$$

This approximation of the magnetic field in a coil of current is called the far-field approximation. Since each vehicle has two coils that are structurally connected to each other, the dipoles created by each coil add into a resultant dipole. If each orthogonal coil is creating a dipole of equal strength, a resultant dipole is pointed diagonally between them with a magnitude equal to $\sqrt{2}$ times their individual magnitudes. This phenomenon allows the EMFF vehicle to steer the dipole by changing the amount of current in each coil. Using the far-field approximation, the testbed layout simplifies to two steerable dipoles, one on each vehicle, as shown in Fig. 6. Additional discussion of the far-field and near-field magnetic models is presented by Schweighart [9]. When the separation distance is twice the coil diameter is the exact field and near field are within 10% of each other.

The magnetic field created by the magnetic dipole on the stationary vehicle μ_s is given by Schwartz [18]

$$\mathbf{B}_S = \frac{\mu_0}{4\pi}\frac{\mu_S}{r^3}[3(\hat{\mu}_S \cdot \hat{\mathbf{r}})\hat{\mathbf{r}} - \hat{\mu}_S] \tag{2}$$

The force and torque experienced by the dipole on the moving vehicle μ_M due to the magnetic field created from the stationary vehicle is given by

$$\mathbf{F} = \mu_M \cdot \nabla \mathbf{B}_S \qquad \mathbf{T} = \mu_M \times \mathbf{B}_S \tag{3}$$

Using Eqs. (2) and (3), the force and torque on a magnetic dipole in the presence of another magnetic dipole can be found. For experimental setup, the stationary vehicle uses a single coil assembly where the magnetic dipole is aligned with the x-axis, as shown in Fig. 6. For this scenario the nonlinear second-order equations describing the dynamics of the moving vehicle can be given as

$$F_x = M\ddot{x} = \frac{3\mu_0\mu_S}{4\pi\sqrt{(x^2+y^2)^7}}(\mu_{M_x}(-2x^3+3xy^2) + \mu_{M_y}(-4x^2y+y^3)) \tag{4}$$

$$F_y = M\ddot{y} = \frac{3\mu_0\mu_S}{4\pi\sqrt{(x^2+y^2)^7}}(\mu_{M_x}(-4x^2y+y^3) + \mu_{M_y}(x^3-4xy^2)) \tag{5}$$

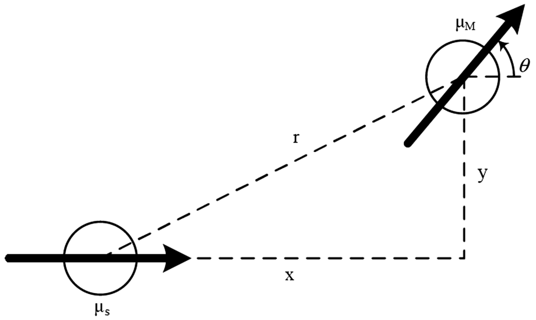

Fig. 6 Testbed setup with far-field approximation.

$$T_z + T_{\mathrm{RW}} = I_z\ddot{\theta} = \frac{\mu_0\mu_S}{4\pi\sqrt{(x^2+y^2)^5}}(\mu_{M_x}(3xy) - \mu_{M_y}(2x^2-y^2)) + T_{\mathrm{RW}} \tag{6}$$

where the magnetic moment of the moving vehicle in the x and y direction is given by

$$\mu_{M_x} = \mu_1\cos\theta - \mu_2\sin\theta \qquad \mu_{M_y} = \mu_1\sin\theta + \mu_2\cos\theta \tag{7}$$

The magnetic moment for each coil on the moving vehicle, μ_1 and μ_2, are adjusted by changing the amount of current in the wire.

B. Control

In two dimensions, a steerable magnetic dipole on one vehicle can provide full position control between itself and a vehicle with a fixed magnetic dipole. However, in implementing this control, torques would be often applied to this vehicle causing it to experience varying degrees of rotation. By adding a reaction wheel to this system, the angular position of the vehicle can be controlled. This method decouples the position and angle control of the EMFF vehicle. The two superconducting coils are used to control the two-dimensional position of the vehicle and the reaction wheel is used to control the angle of the vehicle. This method simplifies the implementation of more complex controllers for the magnetic coils. The torque of the reaction wheel provides an opposite torque on the vehicle to preserve angular momentum. The state-space representation of the angle control system is a simple, standard scheme and the attitude dynamics are given by

$$\begin{bmatrix}\theta \\ \dot{\theta}\end{bmatrix} = \begin{bmatrix}0 & 1 \\ 0 & 0\end{bmatrix}\begin{bmatrix}\theta \\ \dot{\theta}\end{bmatrix} + \begin{bmatrix}0 \\ 1/I_z\end{bmatrix}T_{\mathrm{RW}} \tag{8}$$

In the EMFF system, as separation distance r increases, the electromagnetic force drops off as $1/r^4$ [as seen in Eq. (3)] making the system inherently very nonlinear. Even so, at locations very close to the operating point, the dynamics can be approximated as being linear. For a position hold demonstration, a LQR controller is designed. The control inputs are the current applied to each coil on the moving vehicle and the torque from the reaction wheel. These are given by

$$\mathbf{x} = \begin{bmatrix}x \\ \dot{x} \\ y \\ \dot{y} \\ \theta \\ \dot{\theta}\end{bmatrix} \qquad \mathbf{u} = \begin{bmatrix}i_x \\ i_y \\ T_{\mathrm{RW}}\end{bmatrix} \tag{9}$$

Using Eqs. (4–6), the position and angular accelerations for the moving vehicle are

$$\begin{bmatrix}\ddot{x} \\ \ddot{y} \\ \ddot{\theta}\end{bmatrix} = \begin{bmatrix}\frac{F_x}{M} \\ \frac{F_y}{M} \\ \frac{T_z+T_{\mathrm{RW}}}{I_z}\end{bmatrix} \tag{10}$$

Now that the equations of motion are put into a nonlinear vector function of the state and control input vectors, which has the form $\dot{x} = f(x,u)$, the next step is linearization around a reference position for the position hold demonstration. This has the standard linear model commonly found in control texts [19] as

$$\delta\dot{x} = \left.\frac{\delta f}{\delta x}\right|_{(x_r,u_r)}\delta x + \left.\frac{\delta f}{\delta u}\right|_{(x_r,u_r)}\delta u \qquad \triangleq \mathbf{A}\delta x + \mathbf{B}\delta u \tag{11}$$

and for the EMFF vehicles, the **A** and **B** matrices are modeled as

$$\mathbf{A} = \begin{bmatrix} 0 & 1 & 0 & 0 & 0 & 0 \\ \frac{\partial}{\partial x}\left(\frac{F_x}{M}\right) & \frac{\partial}{\partial \dot{x}}\left(\frac{F_x}{M}\right) & \frac{\partial}{\partial y}\left(\frac{F_x}{M}\right) & \frac{\partial}{\partial \dot{y}}\left(\frac{F_x}{M}\right) & \frac{\partial}{\partial \theta}\left(\frac{F_x}{M}\right) & \frac{\partial}{\partial \dot{\theta}}\left(\frac{F_x}{M}\right) \\ 0 & 0 & 0 & 1 & 0 & 0 \\ \frac{\partial}{\partial x}\left(\frac{F_y}{M}\right) & \frac{\partial}{\partial \dot{x}}\left(\frac{F_y}{M}\right) & \frac{\partial}{\partial y}\left(\frac{F_y}{M}\right) & \frac{\partial}{\partial \dot{y}}\left(\frac{F_y}{M}\right) & \frac{\partial}{\partial \theta}\left(\frac{F_y}{M}\right) & \frac{\partial}{\partial \dot{\theta}}\left(\frac{F_y}{M}\right) \\ 0 & 0 & 0 & 0 & 0 & 1 \\ \frac{\partial}{\partial x}\left(\frac{T_z+T_{\mathrm{RW}}}{I_Z}\right) & \frac{\partial}{\partial \dot{x}}\left(\frac{T_z+T_{\mathrm{RW}}}{I_Z}\right) & \frac{\partial}{\partial y}\left(\frac{T_z+T_{\mathrm{RW}}}{I_Z}\right) & \frac{\partial}{\partial \dot{y}}\left(\frac{T_z+T_{\mathrm{RW}}}{I_Z}\right) & \frac{\partial}{\partial \theta}\left(\frac{T_z+T_{\mathrm{RW}}}{I_Z}\right) & \frac{\partial}{\partial \dot{\theta}}\left(\frac{T_z+T_{\mathrm{RW}}}{I_Z}\right) \end{bmatrix} \tag{12}$$

$$\mathbf{B} = \begin{bmatrix} 0 & 0 & 0 \\ \frac{\partial}{\partial i_x}\left(\frac{F_x}{M}\right) & \frac{\partial}{\partial i_y}\left(\frac{F_x}{M}\right) & \frac{\partial}{\partial T_{\mathrm{RW}}}\left(\frac{F_x}{M}\right) \\ 0 & 0 & 0 \\ \frac{\partial}{\partial i_x}\left(\frac{F_y}{M}\right) & \frac{\partial}{\partial i_y}\left(\frac{F_y}{M}\right) & \frac{\partial}{\partial T_{\mathrm{RW}}}\left(\frac{F_y}{M}\right) \\ 0 & 0 & 0 \\ \frac{\partial}{\partial i_x}\left(\frac{T_z+T_{\mathrm{RW}}}{I_z}\right) & \frac{\partial}{\partial i_y}\left(\frac{T_z+T_{\mathrm{RW}}}{I_z}\right) & \frac{\partial}{\partial T_{\mathrm{RW}}}\left(\frac{T_z+T_{\mathrm{RW}}}{I_z}\right) \end{bmatrix} \tag{13}$$

If the moving vehicle has no current in its coil initially, at the start of a test the **A** matrix is

$$\mathbf{A} = \begin{bmatrix} 0 & 1 & 0 & 0 & 0 & 0 \\ 0 & 0 & 0 & 0 & 0 & 0 \\ 0 & 0 & 0 & 1 & 0 & 0 \\ 0 & 0 & 0 & 0 & 0 & 0 \\ 0 & 0 & 0 & 0 & 0 & 1 \\ 0 & 0 & 0 & 0 & 0 & 0 \end{bmatrix} \tag{14}$$

Given a reference position the **B** matrix can be calculated. By solving an algebraic Riccati equation with **A**, **B**, and appropriately weighting the state error and control variables and taking its steady-state solution, a standard full state feedback control law is obtained

$$\delta u = -\mathrm{K}_{\mathrm{LQR}} \delta x \tag{15}$$

In addition, the state feedback control law for the attitude control has the following form

$$T_{\mathrm{RW}} = -K_\theta \begin{bmatrix} \theta \\ \dot{\theta} \end{bmatrix} \tag{16}$$

Thus, the coil currents i_x and i_y for the position control are determined by $\mathbf{K}_{\mathrm{LQR}}$, and the reaction wheel torque, T_{RW}, for the attitude control is determined by $\mathbf{K}_\theta$. For an estimator an extended Kalman filter with a steady-state gain is developed. Simulations of the linearized model were performed by Neave [15] and indicated that the EMFF testbed was able to control its position to approximately the centimeter-level precision of the metrology system. The maximum current in the coil of 120 amps is a hardware limit modeled by the simulation.

C. Test Settings

The process noise characteristics and sensor noise characteristics used by the demonstration maneuvers are the following:

$$\begin{gathered} \sigma_x^2 = 10^{-6} \qquad \sigma_y^2 = 10^{-6} \qquad \sigma_\theta^2 = 10^{-2} \\ \sigma_{\text{ultrasound}}^2 = 3 \cdot 10^{-2} \qquad \sigma_{\text{gyro}}^2 = 10^{-9} \end{gathered} \tag{17}$$

Statistical data from several calibration experiments were used to determine $\sigma_{\text{ultrasound}}^2$ while σ_{gyro}^2 was found from the gyro data sheet. For the rotational motion tuning, the ratio of σ_θ^2 to σ_{gyro}^2 was set much greater than one so that the filter could rely more on the gyro measurement than on the rotational dynamics. Initial experimental results indicated that the far-field model did not predict rotational behavior as accurately as position or velocity. The gain matrix for the coil current control used for the linear trajectory tests is

$$\mathbf{K}_{\mathrm{LQR}} = \begin{bmatrix} 922 & 2365 & 0 & 0 & 0 & 0 \\ 0 & 0 & -936 & -2949 & 2.56 \cdot 10^{-3} & 2.7 \cdot 10^{-3} \end{bmatrix} \tag{18}$$

and the gain matrix for the reaction wheel control is

$$\mathbf{K}_\theta = [3.0574 \quad 7.6352] \tag{19}$$

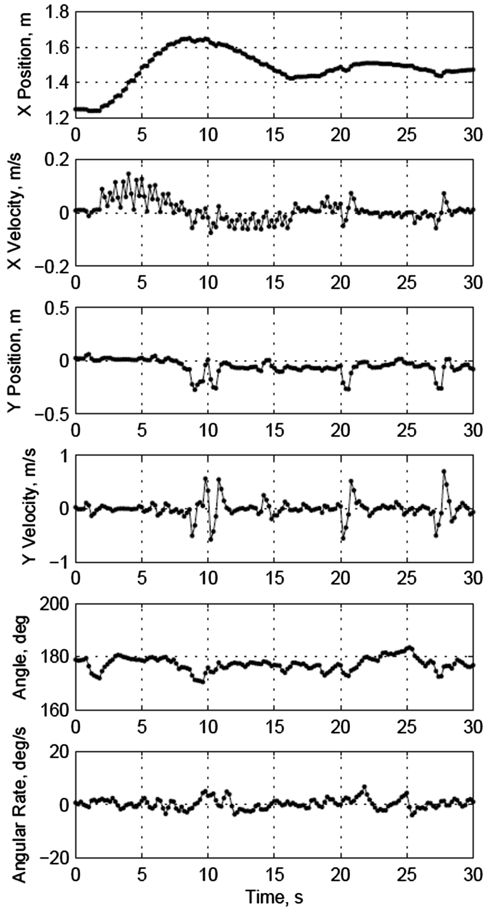

Fig. 7 Step response in *x*-direction.

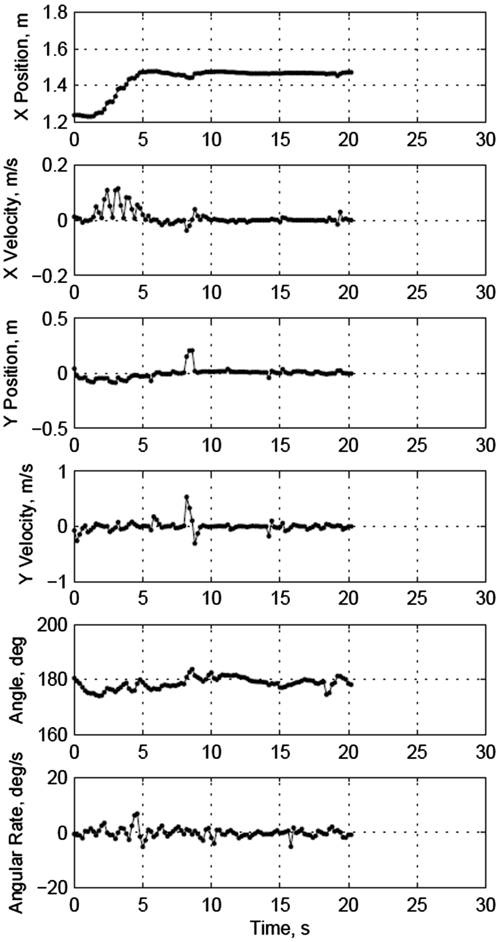

Fig. 8 Step response in x-direction with improved controller.

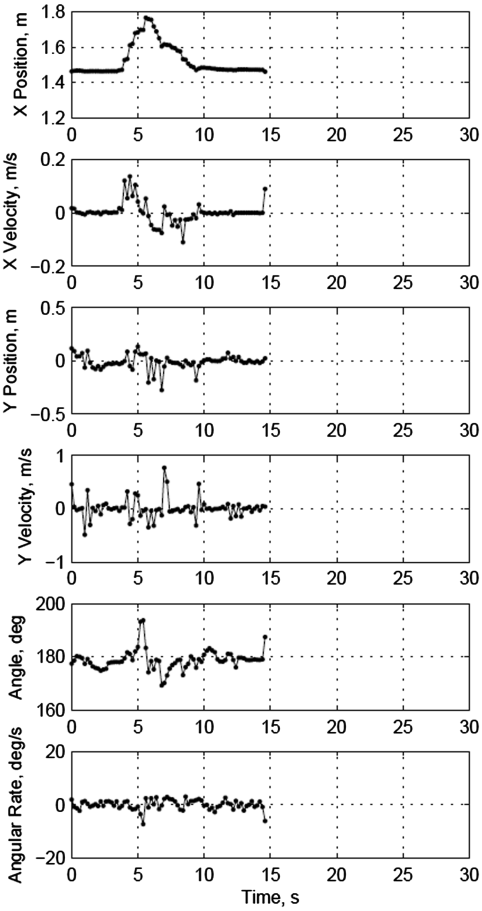

Fig. 9 Impulse response in x-direction.

Several other gain matrices were tested in simulation and results are shown by Neave [15].

V. Position Hold Demonstrations

Initial tests to validate the operation of the EMFF testbed demonstrated open-loop attraction, repulsion, and shear motions. For each test, the current in the coils is held constant at approximately 80 amps and the steady-state power required was approximately 50 watts. Attitude control during maneuvering was maintained by the reaction wheel to prevent the vehicles from spinning during axial attraction and repulsion or shear motions. The first set of closed-loop control demonstrations required the moving vehicle to hold its position at a given reference point while maintaining its attitude. For the tests in this section, the U/S beacons for stationary vehicle were located on the vehicle. To obtain accurate state estimates the tests required an attitude that allowed for the metrology system on the moving vehicle to maintain line of the sight with the stationary vehicle.

The first experiment tested the step response of the moving vehicle in the axial or x-direction. The vehicles were axially aligned with a separation of 1.25 m. The coordinate frame used for testing places the stationary vehicle at the origin and the moving vehicle initially at $x = 1.25$, $y = 0$. The default attitude that is maintained throughout a test is 180°. The reference position was an axially aligned separation of 1.5 m, or $x = 1.5$, $y = 0$. The expected maneuver was for the moving vehicle to move axially to the reference position and this was demonstrated in Fig. 7, which shows each of the elements of the state vector during the test. The first set of plots is the position and velocity in the x-direction. The x position of the moving vehicle starts at 1.25 m and then quickly attempts to move to the reference position, but overshoots. After about 30 s, the vehicle settles at the reference location. The response in the x-direction has 60% overshoot and a 2% settling time of 33 s. The second set of plots in Fig. 7 shows the position and velocity in the y-direction. Minimal deviation was expected along the y-direction and this is shown in Fig. 7. The final set of plots shows the angle and angular rate of the vehicle. Throughout the test the moving vehicle was able to approximately maintain a steady angle.

To decrease the overshoot and settling time, the LQR control gain was modified by first increasing the cost of control and second by decreasing the modeled strength of the electromagnetic force. The tests occurred on an optical bench containing ferromagnetic material under the operating surface causing a potential increase in the electromagnetic force during operation. This was one possible reason for the overshoot in Fig. 7. With the improved controller, the same conditions of the test were repeated and are shown in Fig. 8. Now, the response in the x-direction has no overshoot and the settling time is 9 s, which is a large improvement over the previous settling time of 33 s. Similar to Fig. 7 and as expected, there was minimal deviation for the y and θ states shown in Fig. 8.

In addition to the step response tests, two more position hold experiments were conducted. For these tests, the moving vehicle was initially at the reference position of a 1.5 m separation ($x = 1.5$, $y = 0$) and manually given a push in either the x or y direction to generate an impulse input. The results in Fig. 9 show the position of the vehicle when given a manual push in the x-direction away from the stationary vehicle. The first plot in Fig. 9 shows the moving vehicle pushed away from the stationary vehicle at approximately 4 s and then returning back to the reference position in approximately 5 s. Movement is mostly along the axial direction and attitude is maintained during the test.

The position of the moving vehicle given an impulse in the y-direction is shown in Fig. 10 where the first two plots, showing the x-position and velocity are relatively steady and the second set of plots show the movement in the shear direction. In this case, it takes

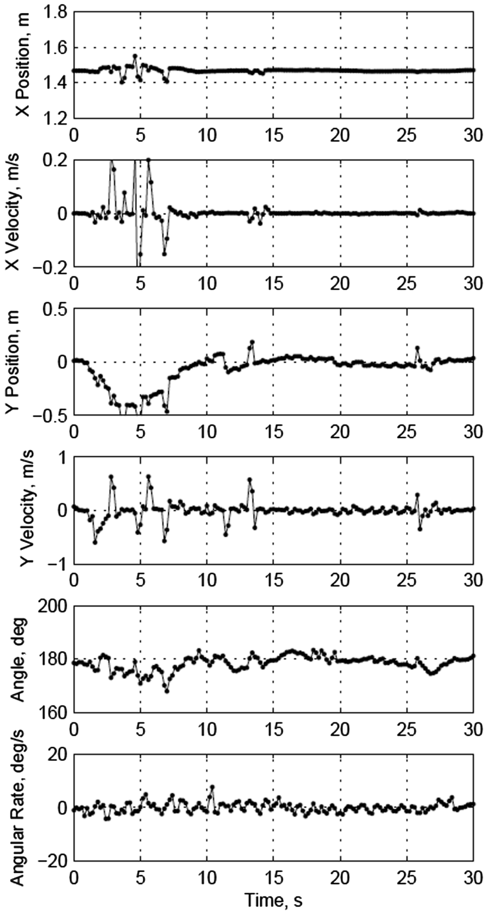

Fig. 10 Impulse response in *y*-direction.

about 10 s for the vehicle to return back to the reference position. The response takes slightly longer potentially because of a larger imparted push in the *y*-direction. Together, the impulse response tests show that the EMFF system is able to return to a reference position given a disturbance.

There were several challenges with testing the EMFF vehicles. Obtaining consistent metrology estimates was a problem during tests and commonly led to errors in position, which then led to an overshoot in position or erratic and jumpy behavior by the electromagnetic actuators or reaction wheel. Some of these effects are seen in the plots of the position hold tests. The cryogenic boiloff of LN_2 was a problem for both the metrology system, as described in Sec. III, and for the air bearing system. The cold vapor caused the air in the plumbing of the air bearing system to freeze leading to stuck or sticky and slow air bearing pucks. Managing consumables during tests was also a challenge. There were three main limiting consumables during testing; the liquid nitrogen for cooling the HTS coils, the batteries for the HTS coils and reaction wheel, and the CO_2 tank for the air carriage system. Individually each had an operational lifetime of about 20 min; however, aligning their lifetimes was a difficult, even at the start of the test. For example, the first time the LN_2 system is filled, only a few tests could be attempted since the LN_2 quickly boiled off. Once the entire vehicle was cold on a second or third refill of LN_2, more tests could be conducted, however, then the air carriage system was too cold for consistent operation. Despite these challenges, in the position hold tests, use of the electromagnetic actuators to control the position showed promising results.

In summary, an experiment for holding the position of a moving EMFF vehicle at a reference point with respect to a stationary vehicle was successfully achieved with an LQR controller and a steady-state Kalman filter estimator. Although the combination of LQR control and a steady-state Kalman filter was sufficient to obtain successful proof-of-concept experimental results for the position hold tests, the pair was not appropriate for a test where the moving vehicle was required to follow a trajectory with respect to the stationary vehicle, especially in terms of the estimator. One problem was that the estimator used the dynamics model linearized about a reference point which was not be able to capture the dynamics along a trajectory.

VI. Trajectory Following Demonstrations

The second set of closed-loop control demonstrations required the moving vehicle to follow a sinusoidal trajectory. To achieve the trajectory following a new scheme was used consisting of a nonlinear controller for the position control, a proportional-integral-derivative (PID) controller, and an extended Kalman filter (EKF) for the estimator. The nonlinear controller for position control was designed for *n*-EMFF satellites in low Earth orbit by Ahsun [20]. Initially, the controller was also used for attitude control, however, problems were encountered because the direct current (DC) motor dynamics included in the attitude controller could not sufficiently model the real dynamic behavior of the RWA. As a solution, an attitude controller using PID and disturbance feed-forward techniques was designed. The DC motor dynamics are given by

$$I_w\dot{\omega} + \frac{K_t}{R_A}V_{\mathrm{emf}}(\omega) + F_f(\omega) = \frac{K_t}{R_A}V \tag{20}$$

where the counterelectromotive force voltage V_{emf} and friction F_f of the motor are functions of ω, the angular velocity of the reaction wheel. As an intermediate variable, $\Phi(\omega)$ is defined as

$$\Phi(\omega) = \frac{K_t}{R_A}V_{\mathrm{emf}}(\omega) + F_f(\omega) \tag{21}$$

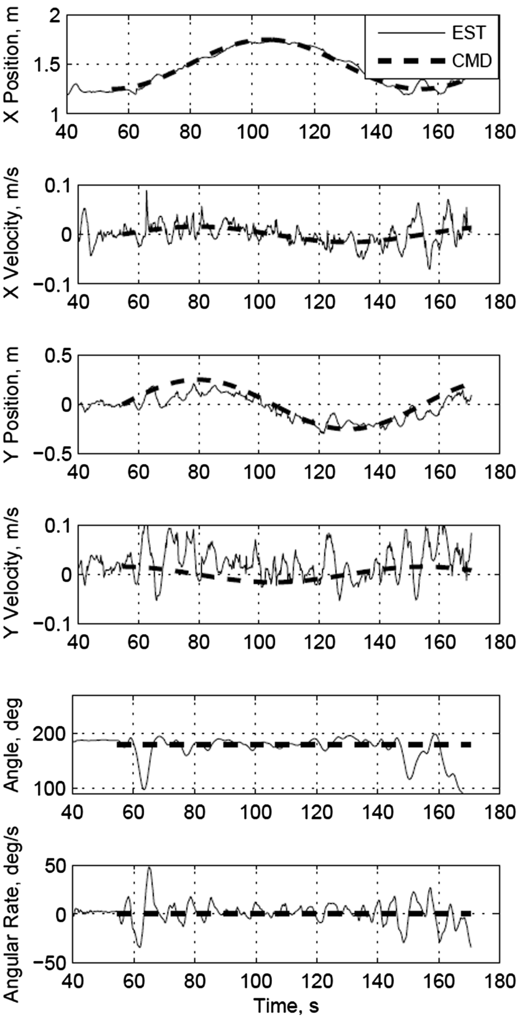

Fig. 11 Circular trajectory.

and values for $\Phi(\omega)$ are obtained by measuring ω in steady state $\dot{\omega} = 0$ for various input voltages so that $\Phi(\omega)$ is modeled as a second-order polynomial of ω. Accounting for the angular momentum conservation of the moving vehicle system, the attitude dynamics including the electromagnetic torque, T_z, is

$$I_z\ddot{\theta} = \Phi(\omega) + T_z - \frac{K_t}{R_A}V \tag{22}$$

The attitude system control law is given by

$$V = \frac{R_A}{K_t}(\Phi(\omega) + T_z) + K_i\int e_\theta\,\mathrm{d}t + K_p e_\theta + K_d\dot{e}_\theta \tag{23}$$

where $e_\theta = \theta_d - \theta$ and maintaining the attitude of the moving vehicle, θ_d, is accomplished by appropriately tuned the gains K_i, K_p, and K_d. Note that V uses feed-forward information of (R_A/K_t) $(\Phi(\omega) + T_z)$.

The estimator for the trajectory control tests uses an extended Kalman filter and the nonlinear measurement vector is given by

$$z_k = \begin{bmatrix} d_{M1} \\ d_{M2} \\ d_{M3} \\ d_{S1} \\ d_{S2} \\ d_{S3} \\ \dot{\theta} \end{bmatrix} = \begin{bmatrix} \sqrt{(x+R\cos\theta)^2 + (y+R\sin\theta)^2} \\ \sqrt{\left(x-R\cos\left(\theta-\frac{\pi}{3}\right)\right)^2 + \left(y-R\sin\left(\theta-\frac{\pi}{3}\right)\right)^2} \\ \sqrt{\left(x-R\cos\left(\theta+\frac{\pi}{3}\right)\right)^2 + \left(y-R\sin\left(\theta+\frac{\pi}{3}\right)\right)^2} \\ \sqrt{(x-R)^2 + y^2} \\ \sqrt{\left(x+R\cos\frac{\pi}{3}\right)^2 + \left(y-R\sin\frac{\pi}{3}\right)^2} \\ \sqrt{\left(x+R\cos\frac{\pi}{3}\right)^2 + \left(y+R\sin\frac{\pi}{3}\right)^2} \\ \dot{\theta} \end{bmatrix} \tag{24}$$

where d_{M_i} is distance from the U/S beacon of the stationary vehicle to the ith U/S receiver of the moving and d_{S_i} is distance from the U/S beacon of the moving vehicle to the ith U/S receiver of the stationary vehicle for $i = 1, 2, 3$. To prevent inaccurate U/S measurements from entering the estimator at each time step, the elements of $\mathbf{z}_k$ were filtered, and $\mathbf{z}_k$ was modified into $\tilde{\mathbf{z}}_k$ so that it contained only accurate U/S measurements and gyro measurement. In addition, the size of $\mathbf{K}_k$ varied in accordance with the size of $\tilde{\mathbf{z}}_k$. If the number of accurate U/S measurements at t_k was zero, then $\hat{\mathbf{x}}_k$ took the values of $\hat{\mathbf{x}}_k^-$ by omitting the update procedure with $\mathbf{z}_k$. Convergence of the estimator was achieved by taking advantage of the redundancy in the measurements [21]. Before filter, it was common for the estimator to receive dozens of bad measurements during a 1 min test preventing a useful demonstration from occurring. With the filtering procedure, the estimator was able to complete the desired trajectory following demonstrations lasting a few minutes.

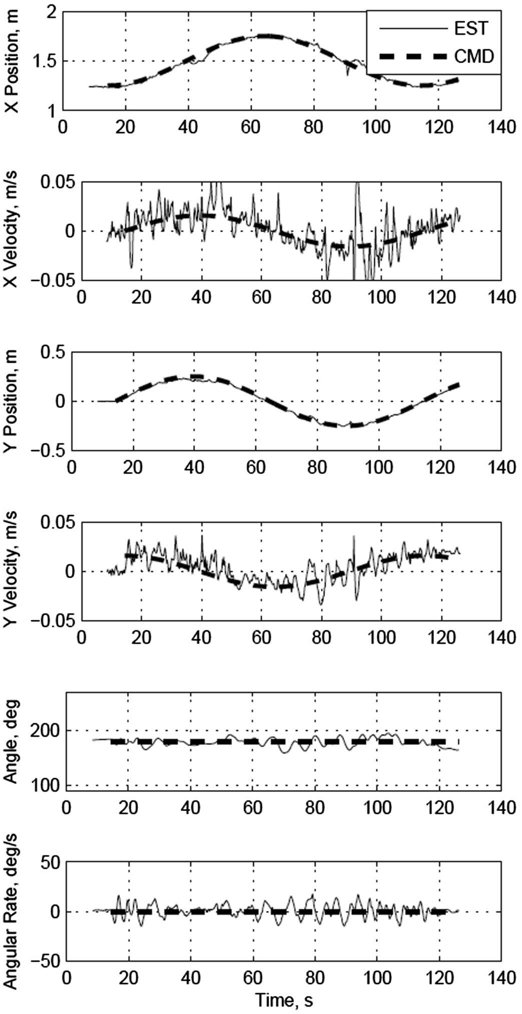

Fig. 12 Circular trajectory after beacon location change.

The desired sinusoidal trajectory for the moving vehicle was given by

$$\begin{aligned} x_d(t) &= x_{\text{center}} - A_x\cos(2\pi f_x(t-t_0)) \\ \dot{x}_d(t) &= 2\pi f_x A_x\sin(2\pi f_x(t-t_0)) \\ y_d(t) &= y_{\text{center}} + \sin(2\pi f_y(t-t_0)) \\ \dot{y}_d(t) &= 2\pi f_y A_y\cos(2\pi f_y(t-t_0)) \\ \theta_d(t) &= \pi \qquad \dot{\theta}_d(t) = 0 \end{aligned} \tag{25}$$

where t_0 is the time when the controller is activated. The results of the first experiment is shown in Fig. 11 and involved a circular trajectory with a radius of 0.25 m and a period of 100 s, where $A_x = A_y = 0.25$ and $f_x = f_y = 0.01$. Similar to the position hold tests, the stationary vehicle is at the origin. The moving vehicle starts at $x = 1.25$ $y = 0$ and rotates around the point $x_{\text{center}} = 1.5$ $y_{\text{center}} = 0$ while maintaining attitude. Figure 11 shows the commanded trajectory (dashed) and the observed trajectory (solid) and the position tracks well in the x-direction. Tracking in the y-direction was not as close. This was because obtaining accurate position estimates was difficult especially in the y-direction and it was observed that there was a larger amount of fluctuation in $\hat{y}$ and $\dot{\hat{y}}$ compared with that of $\hat{x}$ and $\dot{\hat{x}}$.

As a solution, the U/S beacon on the stationary vehicle was moved from on the vehicle to $x = 1.5$, $y = -1.5$, which is shown as the "New Beacon Location" in Fig. 5, as described in Sec. III. With the improved ability of the moving vehicle to estimate its motion along the y-direction, the circular trajectory demonstration was retested and the results are shown in Fig. 12. Now both the x and y positions tracked the commanded trajectory very closely while maintaining attitude and the improvement can be seen in the plot of the y position. A comparison of the trajectories for both the old beacon location test

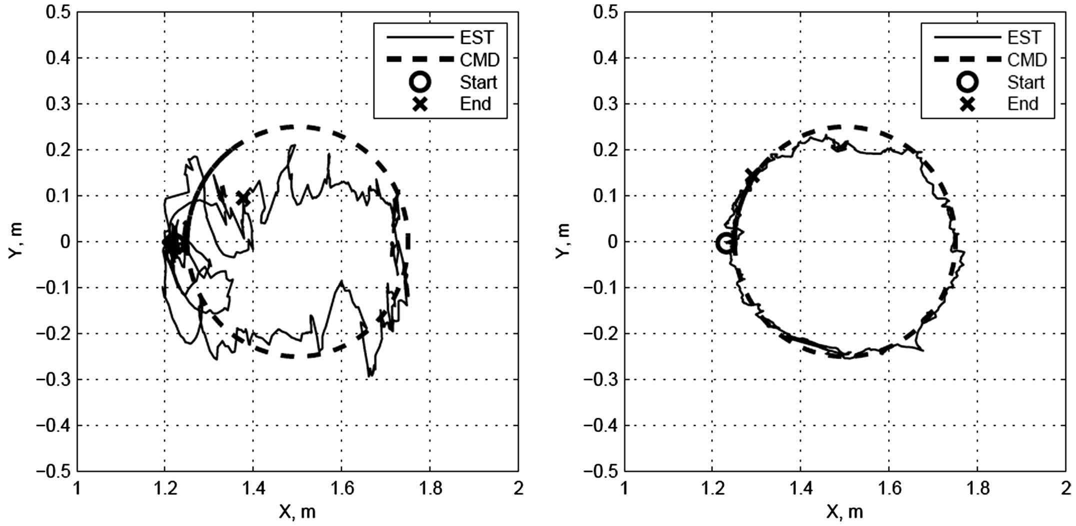

a) Old beacon location **b) New beacon location**

Fig. 13 Circular trajectories in xy-plane.

and the new beacon location test are shown in the xy-plane in Fig. 13. The improvement in performance by simply modifying the experimental setup of the metrology is clearly seen. A more accurate circular trajectory tracking is easily seen by the new beacon location test compared with the old beacon location test. Other tests with circular trajectory have demonstrated a rotational period of 80 s.

For the last set of experiments, a sinusoidal trajectory with asymmetrical frequencies for Eq. (25) was conducted. Here, the desired trajectory along the y direction remained the same as $A_y = 0.25$ and $f_y = 0.01$, but the amplitude and the frequency for the x direction were changed to $A_x = 0.3$ and $f_x = 0.02$, respectively. The commanded and experimentally observed trajectories are shown in the xy-plane in Fig. 14. The elements of the state vector are shown in Fig. 15. The trajectory along the x direction is twice as fast as in the y-direction. The x and y positions are close to the commanded trajectory while maintaining attitude, however, towards the end of the test the angular momentum of the wheel becomes saturated. The reaction wheel loses authority and the vehicle loses attitude control ending the experiment. Once attitude control is lost, the vehicle usually spins uncontrollably in one direction and also translates out of control due to undesired forces and torques that rapidly overcome the moving vehicle. This event also occurred at the end of the first circular trajectory test as seen by the drop in attitude in Fig. 11 after 150 s. One item of future work is integrating a new reaction wheel with a larger moment of inertia so that the increased angular momentum storage is sufficient to counter all the electromagnetic torque produced during any shear motions of the moving vehicle. Another potential solution is to change the motor control interface from a voltage-to-angular velocity to a current-to-motor torque

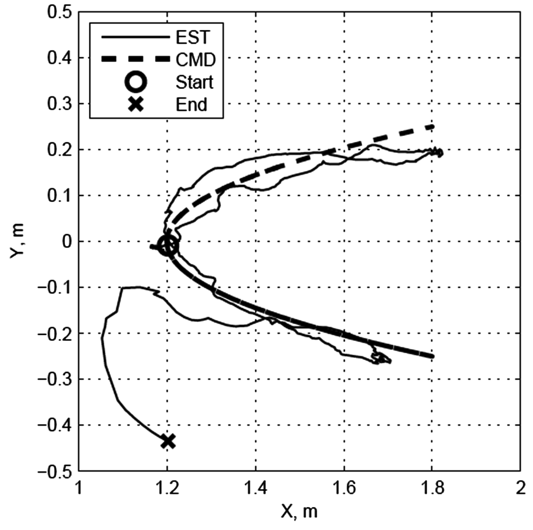

Fig. 14 Asymmetrical frequency in xy-plane.

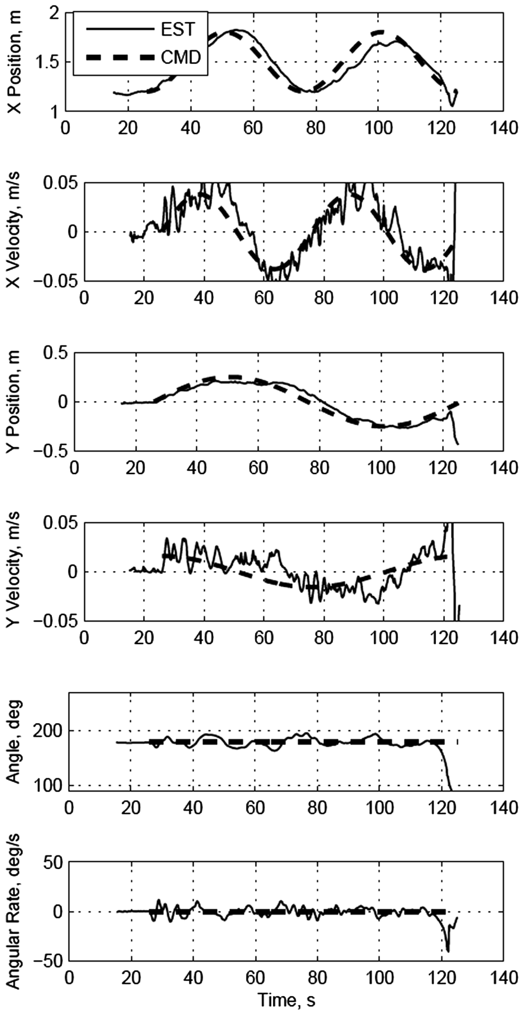

Fig. 15 Asymmetrical frequency.

scheme allowing for attitude control of the vehicle by reaction wheel torque.

VII. Conclusions

Electromagnetic Formation Flight is a unique propellant-free propulsion system for multiple satellite arrays. As a proof-of-concept, two ground testbed vehicles were constructed. The electromagnetic actuators on the testbed are two orthogonal superconducting coils, which are cooled by a liquid nitrogen thermal control system. A reaction wheel is used for attitude control. The vehicles are umbilical-free and consist of avionics, metrology, and power subsystems mounted on a frictionless air bearing system. Using a far-field approximation model for an electromagnetic dipole, the equations of planar motion for the testbed were shown, where a moving vehicle used a steerable dipole and a stationary vehicle used a fixed dipole. This paper describes the first known demonstrations of closed-loop control of the vehicles using the electromagnetic forces in concert with a reaction wheel. Standard control techniques were applied to two sets of demonstrations. The first set of tests involved holding a reference position and used a LQR controller and Kalman filter with steady-state gain. The results show that the moving vehicle returns to a known reference point given a step response and an impulse input. The second set of tests involved following a sinusoidal trajectory. The control scheme used a nonlinear controller for position control, PID controller for attitude control, and an extended Kalman filter with dynamically sized gain. One of the experimental results shows a circular trajectory being tracked. Improvement in the performance of the testbed can be seen by changing the configuration of the metrology system. The results of the demonstrations show that EMFF is a promising actuation system for future formation flight systems.

Acknowledgments

This research was funded in part by the Defense Advanced Research Projects Agency through the Modular Spacecraft Architecture contract with Payload Systems, Inc., Contract #FA945305C0180, administered through the U.S. Air Force Research Laboratory, Albuquerque, New Mexico. The authors would also like to thank David W. Miller for collaborating on the electromagnetic formation flight testbed development.

References

[1] Cockell, C., Leger, A., Fridlund, M., Herbst, T., Kaltenegger, L., Absil, O., "Darwin: A Mission to Detect and Search for Life on Extrasolar Planets," *Astrobiology*, Vol. 9, No. 1, 2009, pp. 1–22. doi:10.1089/ast.2007.0227

[2] Brown, O., and Eremenko, P., "Fractionated Space Architectures: A Vision for Responsive Space," *AIAA 4th Responsive Space Conference*, AIAA Paper RS4-2006-7506, Washington, D.C., 2006.

[3] Schaub, H., "Stabilization of Satellite Motion Relative to a Coulomb Spacecraft Formation," *Journal of Guidance, Control, and Dynamics*, Vol. 28, No. 6, 2005, pp. 1231–1239. doi:10.2514/1.8577

[4] Seubert, C. R., and Schaub, H., "Closed-Loop One-Dimensional Charged Relative Motion Experiments Simulating Constrained Orbital Motion," *AAS/AIAA Astrodynamics Specialist Conference*, AAS Paper 09-390, Pittsburgh, PA, 2009.

[5] Mitchell, J. W., Zakar, D. M., Burns, R. D., and Luquette, R. J., "A Message Oriented Middleware for a Soft Real-Time Hardware-in-the-Loop Spacecraft Formation Flying Testbed," *AIAA Modeling and Simulation Technologies Conference and Exhibit*, AIAA Paper 2006-6127, 2006.

[6] Monda, M. J., and Schaub, H., "Hardware Simulation of Relative Navigation using Visual Sensor Information," *AIAA Guidance, Navigation, and Control Conference*, AIAA Paper 2005-5999, 2005.

[7] Veres, S. M., Lincoln, N. K., and Gabriel, S. B., "Testbed for Satellite Formation Flying Control System Verification," AIAA Paper 2007-2953, 2007.

[8] Romano, M., and Hall, J., "A Test Bed for Proximity Navigation and Control of Spacecraft for On-orbit Assembly and Reconfiguration," *Space 2006*, AIAA Paper 2006-7519, 2006.

[9] Schweighart, S. A., "Electromagnetic Formation Flight: Dipole Solution Planning," Ph.D. Thesis, Space Systems Lab., Rept. 9-05, Massachusetts Inst. of Technology, Cambridge, MA, June 2005.

[10] Beichman, C. A., Woolf, N. J., and Lindensmith, C. A. (eds.), "The Terrestrial Planet Finder (TPF): A NASA Origins Program to Search for Habitable Planets," Jet Propulsion Lab., California Inst. of Technology, 99-003, Pasadena, CA, May 1999.

[11] Elias, L. M., Kwon, D. W., Sedwick, R. J., and Miller, D. W., "Electromagnetic Formation Flight Dynamics including Reaction Wheel Gyroscopic Stiffening Effects," *Journal of Guidance, Control, and Dynamics*, Vol. 30, No. 2, 2007, pp. 499–511. doi:10.2514/1.18679

[12] Wawrzaszek, R., and Banaszkiewicz, M., "Dynamics of 2 and 3 Satellite Formations Controlled by Electromagnetic Forces," *36th COSPAR Scientific Assembly* [CD-ROM], Vol. 3028, COSPAR, Beijing, July 2006.

[13] Ahsun, U., "Dynamics and Control of Electromagnetic Satellite Formations," Ph.D. Thesis, Space Systems Lab., Rept. 12-07, Massachusetts Inst. of Technology, Cambridge, MA, June 2007.

[14] Kong, E. M. C., Kwon, D. W., Schweighart, S. A., Elias, L. M., Sedwick, R. J., and Miller, D. W., "Electromagnetic Formation Flight for Multisatellite Arrays," *Journal of Spacecraft and Rockets*, Vol. 41, No. 4, 2004, pp. 659–666. doi:10.2514/1.2172

[15] Neave, M., "Dynamic and Thermal Control of an Electromagnetic Formation Flight Testbed," S.M. Thesis, Space Systems Lab., Rept. 07-05, Massachusetts Inst. of Technology, Cambridge, MA, June 2005.

[16] Chung, S. J., and Miller, D. W., "Propellant-Free Control of Tethered Formation Flight, Part 1: Linear Control and Experimentation," *Journal of Guidance, Control, and Dynamics*, Vol. 31, No. 3, 2008, pp. 571–584. doi:10.2514/1.32188

[17] Kwon, and Daniel, W., "Electromagnetic Formation Flight of Satellite Arrays," S.M. Thesis, Space Systems Lab., Rept. 2-05, Massachusetts Inst. of Technology, Cambridge, MA, Jan. 2005.

[18] Schwartz, M. S., *Principles of Electrodynamics*, Dover Publications, Inc., New York, 1987.

[19] Bryson, A., and Ho, Y. C., *Applied Optimal Control: Optimization, Estimation, and Control*, Taylor and Francis, Washington D.C., 1975.

[20] Ahsun, U., "Dynamics and Control of Electromagnetic Satellite Formations in Low Earth Orbit," *AIAA Guidance, Navigation, and Control Conference*, AIAA Paper 2006-6590, Aug. 2006.

[21] Lee, S. I., "Design and Implementation of the State Estimator for Trajectory Following of an Electromagnetic Formation Flight Testbed," S.M. Thesis, Space Systems Lab., Rept. 02-08, Massachusetts Inst. of Technology, Cambridge, MA, June 2008.

C. McLaughlin
Associate Editor